New iron tetrazolate frameworks: synthesis temperature effect, thermal behaviour, Mössbauer and magnetic studies

Vanessa Pimenta,[a] Quang Hoang Hanh Le,[a] Lucy Clark,[b] Jérôme Lhoste,[a,*] Annie Hémon-Ribaud,[a] Marc Leblanc,[a] Jean-Marc Grenèche,[a] Gilles Dujardin,[a] Philip Lightfoot[b] and Vincent Maisonneuve.[a]

[a]*IMMM-UMR 6283 CNRS, LUNAM, Faculté des Sciences et Techniques, Université du Maine, Avenue Olivier Messiaen, 72085 Le Mans Cedex 9, France*
[b]*School of Chemistry and EaStChem, University of St. Andrews, St. Andrews, Fife, KY16 9ST, United Kingdom*

[*] To whom correspondence should be addressed. E-mail: jerome.lhoste@univ-lemans.fr Phone: (33).(0)2 43 83 33 59. Fax: (33).(0)2 43 83 35 06

Abstract

The exploration of the FeF_3/FeF_2-H*amtetraz*-HF system in dimethylformamide by solvothermal synthesis evidences two isostructural 3D hybrid fluoroferrates. They are prepared from the same starting mixture at two different synthesis temperatures: 120°C for $[H\mathit{dma}]\cdot(Fe_4^{II}Fe^{III}F_8(H_2O)_2(\mathit{amtetraz})_4)$ (**1**) and 140°C for $[H\mathit{dma}]_{1.5}\cdot(Fe_{4.5}^{II}Fe_{0.5}^{III}F_7(H_2O)(HCOO)(\mathit{amtetraz})_4)$ (**2**). Both compounds are characterized by single crystal X-ray diffraction, X-ray thermodiffraction, TGA analysis and Mössbauer spectrometry and SQUID magnetometry. They crystallize in the monoclinic system and are built up from two distinct chains connected by aminotetrazolate anions. The first chain $_\infty(Fe^{II}FN_4)$ is common to **1** and **2** and can be found in numerous fluorides. In the second chain $_\infty(Fe_3X_{12})$ (X = F, N, O), iron cations adopt both valence states Fe(II)/Fe(III). The hydrolysis of DMF implies the formation of $[H\mathit{dma}]^+$ cation and $(HCOO)^-$ anion. The presence of Fe^{3+} in both phases is evidenced by ^{57}Fe Mössbauer spectrometry. The magnetic properties are studied and two transitions from a paramagnetic regime to a long range ordered state below 30 K and 5 K are identified.

Keywords: hybrid fluorides, tetrazole, solvothermal synthesis, magnetic properties

Introduction

The research of new porous hybrid materials, also known as metal-organic frameworks (MOFs) or porous coordination polymers (PCPs) has received widespread attention in the last decade. Owing to their structural diversity, porous 3D organic-inorganic hybrid compounds exhibit remarkable physical and chemical properties. Depending on the porosity, MOFs can be used as functional materials for a wide range of applications in different fields such as catalysis[1], gas storage[2] and separation[3] or targeted drug delivery.[4] The diverse range of organic linkers and metal ions, with various geometries and connection modes[5] allows the design of new architectures with original topologies. Most of the known compounds involve 3*d* block transition metals (Cr^{3+}, Fe^{3+}, Co^{2+}, Cu^{2+}, Zn^{2+}, ...)[6,7,8,9], nevertheless several frameworks including lanthanides[10] or actinides[11] can be found in the literature. In a previous work, we have demonstrated the possibility of building original 3D networks by including two different metallic centres with distinct oxidation states.[12,13]

Besides the versatility of the metallic cation, the organic linker plays a key role in the preparation of new architectures. Carboxylate molecules are the most common linkers[14,15,16], although phosphonates, sulfonates and specially N-donor molecules are frequently employed.[17,18] Gamez and co-workers[19] described a large variety of structures where triazoles and tetrazoles act as bridging ligands. Tetrazoles have been largely used in bio-chemistry as analogues to carboxylic acids because of the close similarity between their acidic characters.[20] Tetrazoles and tetrazolates have remarkable coordination ability, providing up to ten different connection modes.[21]

Several teams have worked with 5-aminotetrazole, however the described architectures exhibit exclusively divalent cations and no examples of mixed valence.[22,23,24,25] Aminotetrazole is a multifunctional ligand and the reported structures present several properties. You and co-workers[26] report the hydrothermal synthesis of two Mn^{2+} hybrid structures displaying ferromagnetic behaviour.

The porous nature of the metal-organic frameworks seems to weaken the magnetic interactions. In fact, the connectivity between the metallic cations takes place through diamagnetic linkers. Their presence can inhibit the orbital overlap between the nearest neighbouring moment-carrying metal centres and limit the strong long-range interactions. Kurmoo *et al.*[27] have shown that architectures built up from chains or layers of moment-carrying transition metals, in which the connection between these entities is ensured by M-O-M bonds, display magnetic properties. Another possible strategy to increase the tridimensional connectivity of the chemical interactions is to link corner-sharing transition metal chains through the intermediary of rigid organic linkers with delocalized π electrons.[28]

Mixed-valence iron hybrid fluorides are very rarely described in literature[29,30] and recently we have reported the synthesis of a hybrid fluoroferrate[31], Fe_2F_5(H*taz*) which exhibits Fe^{II}/Fe^{III} valence states (H*taz* stands for 1,2,4-triazole). The present paper will focus on the synthesis of two isostructural iron frameworks, the effect of temperature on their formulation and their structural description. Their thermal behaviour and the magnetic properties are also studied.

Experimental section

Synthesis

The starting reactants were FeF_2 (prepared from a mixture of Fe + $2FeF_3$ at 850°C during 3 h), FeF_3 (≥99.9%, Alfa Aesar), hydrofluoric acid solution 4% (prepared from 40% HF, Riedel De Haen), 5-aminotetrazole (H*amtetraz*) (98%, Alfa Aesar) and dimethylformamide (DMF) (99.8%, Sigma Aldrich). The solvothermal syntheses were carried out in a 25 mL Teflon-lined stainless steel Parr autoclave under autogenous pressure. The compounds were prepared from the same mixture: FeF_2 (35 mg, 0.37 mmol), FeF_3 (42 mg, 0.37 mmol), HF 2.28 $mol.L^{-1}$ (2.63 mL, 6.0 mmol), 5-aminotetrazole monohydrate (7.7 mg, 0.75 mmol) and DMF (5.0 mL, 64.50 mmol) in molar proportions 1/1/16/2/174. Only the synthesis temperature changed for **1** and **2**. The final products were washed with DMF, filtered and dried at room temperature. The crystalline purity of **1** and **2** was confirmed by X-ray powder diffraction (Figure S1).

$[H\mathit{dma}]\cdot(Fe_4^{II}Fe^{III}F_8(H_2O)_2(\mathit{amtetraz})_4)$ (**1**) was obtained after 72 h at 120°C ($[H\mathit{dma}]^+$ = dimethylammonium cation). The rods, observed from scanning electronic microscopy (SEM), are spherically grouped (Fig. 1 left). $[H\mathit{dma}]_{1.5}\cdot(Fe_{4.5}^{II}Fe_{0.5}^{III}F_7(H_2O)(HCOO)(\mathit{amtetraz})_4)$ (**2**) was obtained after 72 h at 140°C. SEM images show brush-like needles (Fig. 1 right). $[H\mathit{dma}]^+$ and $[HCOO]^-$ result from the hydrolysis of DMF solvent at high temperature: [32,33]

$$(CH_3)_2N\text{-}CHO + H_2O \rightarrow (CH_3)_2NH_2^+ + HCOO^-$$

The synthesis performed at 160 °C leads to **2** with two extra impurities $[CN_3H_6]_3\cdot(FeF_6)$ and $[NH_4]_3\cdot(FeF_6)$, issued from aminotetrazole decomposition (Figure S2).[34] For lower temperatures (< 120°C) or different mixture compositions, large quantities of iron starting reactants were found.

X-ray single-crystal and powder diffraction

Single crystals were selected under a polarizing optical microscope and mounted on a MicroMount needle (MiTeGen). X-ray intensity data were collected on a Bruker APEX II Quazar diffractometer (4-circle Kappa goniometer, IμS microfocus source (Mo Kα), CCD detector) at 150 K for **1** and at 296 K for **2**. The structures were determined by direct methods with SHELXS-97 and SHELXL-97 programs included in WINGX package.[35,36] The positions of amine hydrogen atoms were geometrically constrained (HFIX options). The final refinements include anisotropic thermal parameters of all non-hydrogen and were performed using the SHELX program on the basis of F^2. The $[H\mathit{dma}]^+$ cations were located from the Fourier difference map. However, all hydrogen atoms of disordered entities (water molecules, formate and H*dma* ions) were not located. The conditions of crystal data collection are listed in Table 1. The atomic coordinates are presented in Supplementary Information. The assignments of the atoms in metal environments were based on M-(O/F/N) distances, thermal motion considerations and valence bond analysis (Table 2).[37,38,39] The exact formulations of compounds have been determined from X-ray diffraction data and ^{57}Fe Mössbauer spectrometry. Crystallographic data (excluding structure factors) for the structures of **1** and **2** have been deposited with the Cambridge Crystallographic Data Centre as supplementary publication nos. CCDC 1024955 ($[H\mathit{dma}]\cdot(Fe_4^{II}Fe^{III}F_8(H_2O)_2(\mathit{amtetraz})_4)$ (**1**)) and 1024954 ($[H\mathit{dma}]_{1.5}\cdot(Fe_{4.5}^{II}Fe_{0.5}^{III}F_7(H_2O)(HCOO)(\mathit{amtetraz})_4)$ (**2**)). Copies of the data can be obtained, free of charge, on application to CCDC, 12 Union Road, Cambridge CB2 1EZ, UK, (fax: +44 1223 336033 or e-mail: deposit@ccdc.cam.ac.uk).

Thermal analysis

Thermal analyses were performed with a SETARAM TGA 92 thermo analyzer under O_2 flow with a heating rate of $3°C \cdot min^{-1}$ from room temperature up to 900°C. X-ray thermodiffraction was carried out under air from 40 to 600°C in an Anton Paar XRK 900 high temperature furnace using a Panalytical X'Pert Pro diffractometer (CuK_α radiation). The samples were heated with a heating rate of $10°C.min^{-1}$ at 10°C intervals from room temperature to 400°C and at 50°C intervals up to 600°C. X-ray diffraction (XRD) patterns were collected in the 5–60° 2θ range with a scan time of 10 min.

Mössbauer Spectrometry

Mössbauer experiments were performed in transmission geometry with a 925 MBq γ-source of $^{57}Co/Rh$ mounted on a conventional constant acceleration drive. The samples consisted of a thin layer of powder containing 5 mg Fe/cm^2. The Mössbauer spectra were recorded at 300 K and at 77 K using a bath cryostat. They were fitted using the MOSFIT program[40], involving quadrupolar components with Lorentzian lines; the isomer shift values are referred to that of α-Fe at 300 K.

Magnetic measurements

Magnetic susceptibility data were collected on a Quantum Design MPMS SQUID magnetometer. Data were recorded in applied fields of 0.1 T and 1 T whilst warming the sample from 2 to 300 K, following consecutive zero-field cooled (ZFC) and field cooled (FC) cycles. The data were corrected for the diamagnetic and background contributions.[41]

Results

Structure description

The structures of **1** and **2** exhibit two types of chains $_\infty(Fe^{II}FN_4)$ and $_\infty(Fe_3X_{12})$ (X = O, F, N) oriented along the *a* axis and connected alternatively by $[amtetraz]^-$ anions according to [011] and $[0\bar{1}1]$ directions (Fig. 2 and Fig. 3). The association of these chains leads to a 3D anionic framework with pseudo square tunnels in which the $[Hdma]^+$ cations are disordered.

The first chain $_\infty(Fe^{II}FN_4)$ results from the condensation of $Fe^{II}F_2N_4$ octahedra by opposite fluorine corners (Fig. 4 top). Each iron atom is surrounded by two axial fluorine atoms and four equatorial nitrogen atoms of four distinct amines. This *trans*-chain with $FeFX_4$ topology is already described in the literature in other fluoroferrates with $_\infty(Fe^{III}F_5)^{2-}$ chains.[42,43]

The second chain $_\infty(Fe_3X_{12})$ (X = F, N or O) displays an architecture that has been encountered in few fluoride hybrids.[44,45] In **1**, the $Fe^{II}{}_2F_5N_4O$ dimers, resulting from two edge-sharing octahedral $Fe^{II}N_2F_3O$ units, are connected to $Fe^{III}F_5O$ monomers by the four equatorial fluorine atoms of adjacent octahedra; the formulation of the chain is $_\infty(Fe^{III}Fe^{II}{}_2F_6O_2N_4)$ (Fig. 4 centre). F/O disorders equal to 0.5/0.5 have been introduced on the axial position F(4)/Ow(4) atoms of $Fe^{III}F_5O$ and on the two edge-sharing atoms F(3)/Ow(3) of the dimeric entities. Both the Fe-F distances and Mössbauer analysis imply the valence II for the Fe(1), Fe(2) and Fe(3) atoms and the valence III for the Fe(4) atom. In **2**, the connection

between the $Fe^{II}_2F_{4.5}N_4O_{1.5}$ dimers and $(Fe^{II}_{0.5}Fe^{III}_{0.5})F_{4.5}O_{1.5}$ octahedra, already observed in **1**, is ensured by equatorial fluorine atoms to give $_\infty(Fe^{II}_{2.5}Fe^{III}_{0.5}F_5O_3N_4)$ chains (Fig. 4 bottom). These entities are equally linked by bridging formate anions arising from DMF decomposition; the carbon atoms are statistically distributed (τ=0.5) to avoid the interpenetration of $[H\textit{dma}]^+$ cations and $(HCOO)^-$ anions. The oxygen atoms are located on F(3)/Ow(3) and F(4)/Ow(4) sites giving F/O disorders equal to 0.25/0.75. Finally, in the $FeF_{4.5}O_{1.5}$ octahedra, the Fe(4) site comprises Fe^{II}/Fe^{III} sites (0.5/0.5) as evidenced by ^{57}Fe Mössbauer spectrometry while valence II is observed for the other iron atoms.

The proposed formulations are in good agreement with the differences in synthesis temperatures. At high temperatures DMF hydrolyses into dimethylammonium and formate anion. The increase of synthesis temperature at 140°C implies a significant solvent decomposition and a reductive media for metal cations. Consequently, **2** contains $HCOO^-$ anions and more $[H\textit{dma}]^+$ cations and iron(II) compared to **1**.

Characterization of 1 and 2

The thermogravimetric curves of **1** and **2** are very similar and show three decomposition steps (Fig. 5). The first weight loss between 25 and 210°C corresponds to the dehydration of **1** (exp.:4.3%, calc.:4.2%). The loss of water molecule and formate decomposition is assumed at 230°C for **2** (exp.: 6.9%, calc.: 7.3%). Then, the second weight loss is attributed to the elimination of amine compounds and HF gas up to 360°C for **1** (exp.: 41.8%, calc.: 42.3%) and **2** (exp.: 41.4%, calc.: 41.2%) to form an amorphous phase that is supposed to be close to FeOF. Above this temperature, a slow hydrolysis of iron oxyfluoride leads to the formation of α-Fe_2O_3 hematite (**1** exp.: 6.3%, calc.: 6.5%, **2** exp.: 5.9%, calc.: 6.2%). X-ray thermodiffraction experiments on **1** and **2** (Fig. 5) are in good agreement with TGA analyses. They indicate three domains: hybrid compound, amorphous phase and hematite. It must be noted that in the first domain, the diffraction peaks shift to higher angles when the temperature increases and the decrease of the cell volume is due to elimination of water and formate entities. At 210°C or 230°C, the resulting structures exhibit probably a small porosity; calculations give 5 % and 2 % porosity, respectively (PLATON program[46]).

Mössbauer spectrometry

The Mössbauer spectra obtained at 300 K and at 77 K on samples **1** and **2** are illustrated in Fig. 6. They exhibit clearly complex hyperfine structures resulting from unresolved quadrupolar features with broadened and non-homogeneous lines: the decomposition into several quadrupolar components is not *a priori* unique. A first question concerns the presence of any preferential orientation in the samples favouring some asymmetry in the quadrupolar hyperfine structures: by rotating the sample with respect to the γ-beam, such an effect is clearly excluded as the hyperfine structure is unchanged. Then the visual description of each spectrum allows *a priori* the presence of both trivalent and divalent Fe species to be concluded. The proportions of the Fe^{3+} content resulting from the difference in absorption area between low and high velocity peaks are unambiguously estimated at 20% and 10% at both temperatures for samples **1** and **2**: this result for sample **1** is in fair agreement with that

obtained from X-ray diffraction while that of sample **2** did originate some further refinement of X-ray diffraction pattern, as is discussed in the previous section. The last step consists of refining the hyperfine structures by means of a minimum number of quadrupolar doublets and to establish physical correlations between 300 K and 77 K data for each sample, and structural correlation between both samples. A modelling based on 4 and 5 quadrupolar components has been successfully obtained for samples **1** and **2**, respectively; the corresponding values of the hyperfine parameters are listed in Table 3. The values of the isomer shift are clearly consistent with mixed-valency states samples, with the presence of high spin Fe^{3+} and Fe^{2+} species. The proportions of each Fe species which were refined for sample **1** without any constraints during the fitting procedure are found to be in excellent agreement with those estimated from X-ray diffraction. On the contrary, some fitting constraints had to be considered for sample **2** to get respective proportions of each Fe^{2+} species to compare well with the crystallographic data. It is important to emphasize that we assumed the same values of recoilless Lamb-Mössbauer factors for both Fe components. In Table 3, we also assigned each quadrupolar component to each Fe^{2+} site by comparing their change from sample **1** to sample **2**. Despite a pure description originating directly from the fitting procedure, the Mössbauer study of these two samples allows us to confirm their mixed-valence state with high spin Fe^{3+} and Fe^{2+} species, to estimate accurately the amount of Fe^{3+} species, to distinguish 3 and 4 iron species, respectively, and to assign all components to the crystallographic sites.

Magnetic properties

The magnetic and inverse susceptibilities of **1** and **2** measured in a 1 T field over the temperature range 2–300 K are shown in Fig. 7(a) and (c), respectively. At high temperatures the data for both samples follow Curie-Weiss behaviour.

A Curie-Weiss fit to the inverse susceptibility data of **1** between 100–300 K yields a molar Curie constant $C_M^{exp.} = 17.96(3)$ and a Weiss constant θ = –96.4(6) K which indicates the dominance of strong antiferromagnetic exchange interactions. The value of this experimental Curie constant is very close to the theoretical value $C_M^{th.} = 16.37$ per formula unit as established from the structure identified by X-ray crystallography and Mössbauer studies of 4 high spin Fe^{2+} and 1 high spin Fe^{3+} per formula unit with spin-only values. The difference implies a small orbital angular momentum contribution to the magnetic moment from Fe^{2+}.[47] Below 100 K, the magnetic susceptibility of **1** begins to deviate from Curie-Weiss behaviour and an increase in the susceptibility can be observed in Fig. 7(a) under ~ 50 K. Fig. 7(b) shows the low temperature susceptibility of **1** in greater detail which was measured in applied fields of 0.1 T and 1 T. The field dependence of the susceptibility indicates that a ferromagnetic component appears below ~ 30 K. It must be noted that the FC and ZFC behaviours differ below ~5 K (inset of Fig. 7(a)).

The magnetic behaviour of **2** is very similar to that of **1**. The fitted values of the susceptibility in Fig. 7(c), give $C_M^{exp.} = 18.33(3)$ and θ = –88.9(4) K, such that $C_M^{exp.}$ is again consistent with the spin-only value with an orbital contribution. In addition, **2** also undergoes a transition below ~ 30 K (Fig. 7(d)) and the FC and ZFC behaviours also differ below ~5 K (inset of Fig.

7c). It is concluded from the current data that **1** and **2** undergo two magnetic ordering transitions. As outlined above, the structures of both **1** and **2** consist of two distinct chains, the first composed of only Fe^{2+} and the second composed of Fe^{2+} and Fe^{3+} or Fe^{2+} and mixed valence Fe^{2+}/Fe^{3+} sites. It is likely that the origin of the two magnetic ordering transitions observed in the susceptibility data at ~ 30 K and 5 K stems from two different ordering mechanisms within the separate chains. It should also be pointed out that Fe^{3+} sites in **1** and the Fe^{2+}/Fe^{3+} sites in **2** form a geometrically frustrated triangular network, such that competition of exchange interactions between neighbouring iron sites may also have a role to play in the magnetic behaviour observed at low temperatures. A common method used to measure magnetic frustration in a material is to calculate the frustration index, $f = |\theta|/T_C$, which compares the energy scale of magnetic interactions given by the magnitude of the Weiss constant, θ, with the energy scale of magnetic order given by the ordering temperature T_C. A value of $f > 1$ indicates spin frustration whereas a conventional non-frustrated system typically has $f \sim 1$.[48] Certainly, if one calculates frustration indices for the two ordering transitions in **1** and **2** and at $T_{C1} \sim 30$ K and $T_{C2} \sim 5$ K the resulting values of $f_1 \sim 3.2$ and 3.0 and $f_2 \sim 19.3$ and 17.8 confirm that strong magnetic frustration exists within **1** and **2**, respectively. From the current data, it is not clear whether the magnetic state of **1** and **2** is weakly ferromagnetic or ferrimagnetic below 30 K.

A future study of these two new materials by powder neutron diffraction could prove very useful as one could study the evolution of magnetic Bragg peaks upon cooling and determine the magnetic ground state through symmetry analysis and magnetic Rietveld refinement. Similarly Mössbauer studies should be performed at low temperature in order to determine the magnetisation at the various iron sites: Fe^{2+} and Fe^{3+} in **1** or Fe^{2+} and mixed Fe^{2+}/Fe^{3+} in **2**.

Conclusion

Two new iso-structural frameworks have been identified at 120 and 140 °C, respectively, $[H\textit{dma}]\cdot(Fe_4^{II}Fe^{III}F_8(H_2O)_2(\textit{amtetraz})_4)$ (**1**) and $[H\textit{dma}]_{1.5}\cdot(Fe_{4.5}^{II}Fe_{0.5}^{III}F_7(H_2O)(HCOO)(\textit{amtetraz})_4)$ (**2**). In this work we have shown that the temperature plays a crucial role in the synthesis of these hybrid organic-inorganic compounds. When the synthesis temperature increases, the solvent is progressively hydrolyzed and in the structure of **2** two fragments can be found, $[H\textit{dma}]^+$ and $HCOO^-$. The presence of Fe^{3+} in both phases is evidenced by ^{57}Fe Mössbauer spectrometry. Upon cooling **1** and **2** undergo two magnetic transitions below 30 K and 5 K. The effective magnetic moments extracted for both systems from the paramagnetic region of their magnetic susceptibility data are consistent with the experimentally derived iron content and valence states.

TABLES

Table 1. Summary of crystallographic data for the structures of fluoroferrate complexes [H*dma*]·($Fe_5F_8(H_2O)_2$(*amtetraz*)$_4$) (**1**) and [H*dma*]$_{1.5}$·($Fe_5F_7(H_2O)$(HCOO)(*amtetraz*)$_4$) (**2**).

		1	**2**
Formula		$Fe_5F_8O_2C_6N_{21}H_{20}$	$Fe_5F_7O_3C_8N_{21.5}H_{23}$
Formula weight		849.47	880.76
Temperature/K		150	296
Crystal size/mm		0.03 x 0.08 x 0.16	0.02 x 0.05 x 0.07
Crystal system		monoclinic	
Space group		*P*2/*m*	
a/Å		6.669(1)	6.612(1)
b/Å		12.245(1)	12.433(2)
c/Å		9.030(2)	8.808(2)
β/°		110.44(1)	107.72(1)
Volume/Å^3		691.0(1)	689.6(1)
Z, $\rho_{calculated}$/g.cm^{-3}		1, 2.042	1, 2.121
μ/mm^{-1}		2.665	2.672
Θ range/°		3.3 – 61.2	3.2 – 56.6
Limiting indices		$-9 \le h \le 9$ $-17 \le k \le 17$ $-12 \le l \le 12$	$-8 \le h \le 8$ $-16 \le k \le 16$ $-10 \le l \le 11$
Collected reflections		16982	16829
Unique reflections [R(int)]		1269	1355
Parameters		112	131
Goodness-of-fit on F^2		1.06	1.14
Final R indices [I>2σ(I)]	R1	0.0852	0.0389
	wR2	0.2212	0.1027
R indices (all data)	R1	0.1502	0.0633
	wR2	0.2614	0.1130
Largest diff. peak and hole/e.Å^{-3}		2.08 and -1.10	0.91 and -0.47

Table 2. Selected inter-atomic distances (Å) and bond valence calculations for fluoroferrate complexes **1** and **2**. *n* corresponds to the number of bonds, taking into account the F/O disorder.

	n	**1**			*n*	**2**		
i-j		d_{ij}	s_{ij}	Σ_{sij} (Fe)		d_{ij}	s_{ij}	Σs_{ij} (Fe)
Fe(1)-F(1)	*2*	2.001(11)	0.39	2.02	*2*	2.011(3)	0.38	2.01
Fe(1)-N(2)	*4*	2.201(11)	0.31		*4*	2.199(3)	0.31	
Fe(2)-F(1)	*2*	2.051(12)	0.42	1.92	*2*	2.033(3)	0.36	2.03
Fe(2)-N(1)	*4*	2.157(10)	0.27		*4*	2.178(3)	0.33	
Fe(3)-F(2)	*2*	2.058(6)	0.42	2.17	*2*	2.016(2)	0.37	1.95
Fe(3)-F(3)	*1*	2.132(5)	0.27		*0.5*	2.181(3)	0.24	
Fe(3)-Ow(3)	*1*	2.132(5)	0.34		*1.5*	2.181(3)	0.30	
Fe(3)-N(4)	*2*	2.146(6)	0.36		*2*	2.189(3)	0.32	
Fe(4)-F(2)	*4*	1.930(5)	0.51	3.14	*4*	2.025(2)	0.36	2.10
Fe(4)-F(4)	*1*	1.940(10)	0.49		*0.5*	2.127(5)	0.28	
Fe(4)-Ow(4)	*1*	1.940(10)	0.61		*1.5*	2.127(5)	0.35	

Table 3. Refined values of hyperfine parameters characteristics of **1** and **2** at 300 K and 77 K: δ, Γ, Δ and % correspond to isomer shift, half-width at half height quadrupolar splitting and relative absorption area, respectively.

	300K				77K			
	δ (mm/s) ±0.02	Γ (mm/s) ±0.02	Δ (mm/s) ±0.05	% ±2	δ (mm/s) ±0.02	Γ (mm/s) ±0.02	Δ (mm/s) ±0.05	% ±2
1	1.11	0.29	3.44	41	1.22	0.40	3.67	39
	1.20	0.44	2.39	20	1.31	0.40	3.14	20
	1.23	0.44	1.83	20	1.32	0.40	2.66	20
	0.41	0.35	0.43	19	0.53	0.38	0.35	21
2	1.10	0.34	3.42	40	1.23	0.55	3.65	40
	1.24	0.30	2.68	19	1.30	0.41	3.34	19
	1.23	0.38	1.80	20	1.32	0.38	2.94	21
	1.25	0.28	2.95	11	1.32	0.45	2.47	11
	0.40	0.32	0.41	10	0.50	0.50	0.35	10

FIGURES

Fig. 1. SEM images of **1** (top) and **2** (bottom).

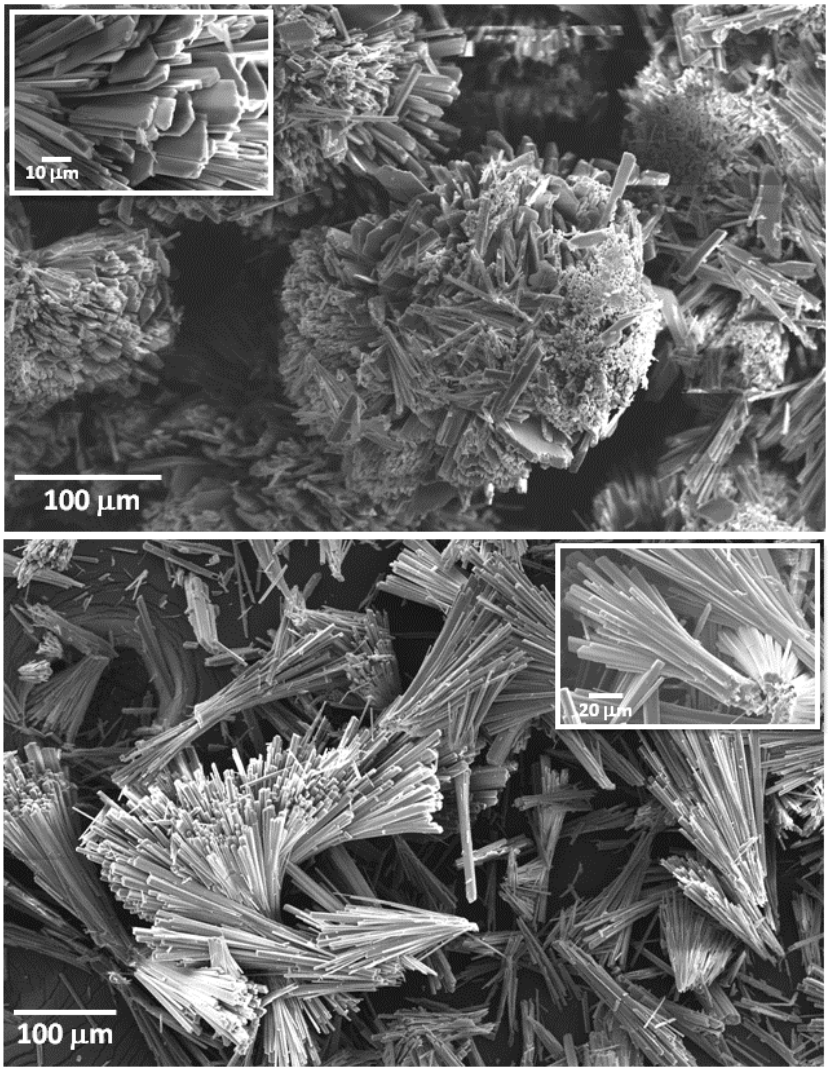

Fig. 2. [100] projection of the 3D network resulting from the connection of $_{\infty}(Fe^{II}FN_4)$ and $_{\infty}(Fe_3X_{12})$ (X = O, F, N) chains in [H*dma*]·($Fe_5F_8(H_2O)_2$(*amtetraz*)$_4$) (**1**) and [H*dma*]$_{1.5}$·($Fe_5F_7(H_2O)$(HCOO)(*amtetraz*)$_4$) (**2**)..

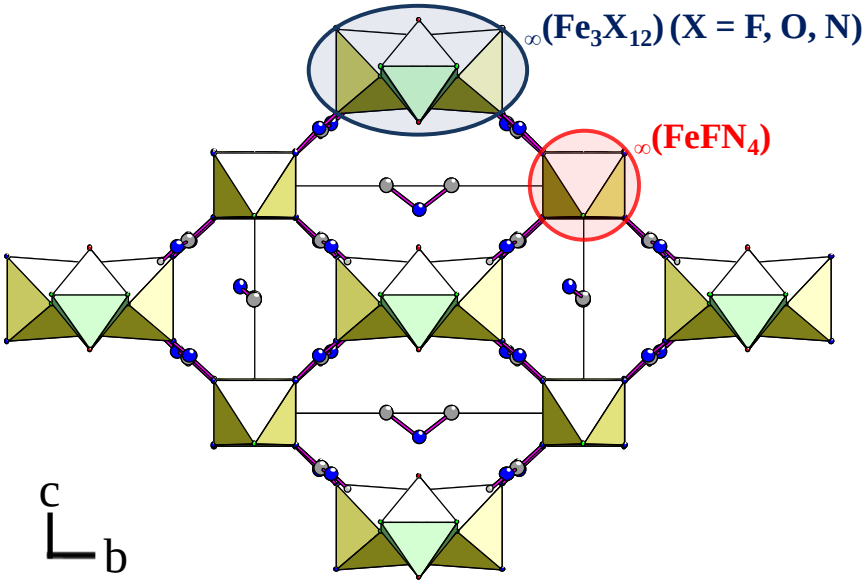

Fig. 3. Bridging mode of aminotetrazolate anion that connect the $_{\infty}(Fe^{II}FN_4)$ and $_{\infty}(M_3X_{12})$ chains in **1** and **2**.

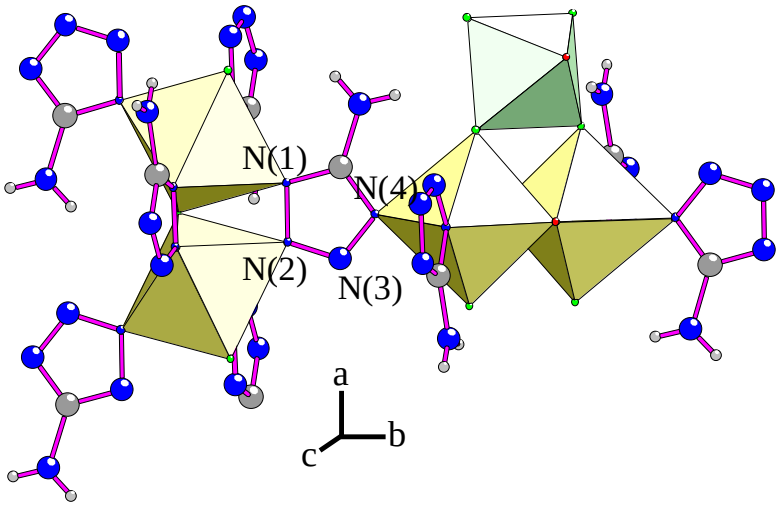

Fig. 4. View of *trans*-chain $_{\infty}(Fe^{II}FN_4)$ in **1** and **2** (top), chain $_{\infty}(Fe^{II}Fe^{III}{}_2F_6O_2N_4)$ (center) in **1** and $_{\infty}(Fe^{II}{}_{2.5}Fe^{III}{}_{0.5}F_5O_3N_4)$ in **2** (bottom).

$_{\infty}(Fe^{II}FN_4)$ in **1** and **2**

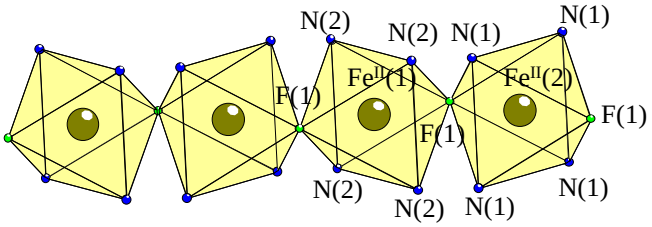

$_{\infty}(Fe^{II}{}_2Fe^{III}F_6O_2N_4)$ in **1**

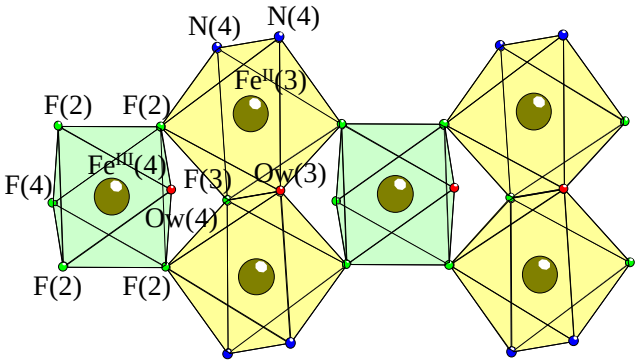

$_{\infty}(Fe^{II}{}_2(Fe^{II}{}_{0.5}/Fe^{III}{}_{0.5})F_5O_3N_4)$ in **2**

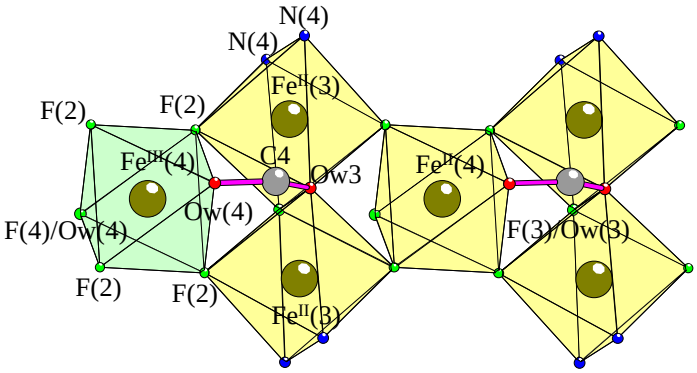

Fig. 5. TGA and thermal evolution of the X-ray diffractograms under air atmosphere of **1** (top) and **2** (bottom).

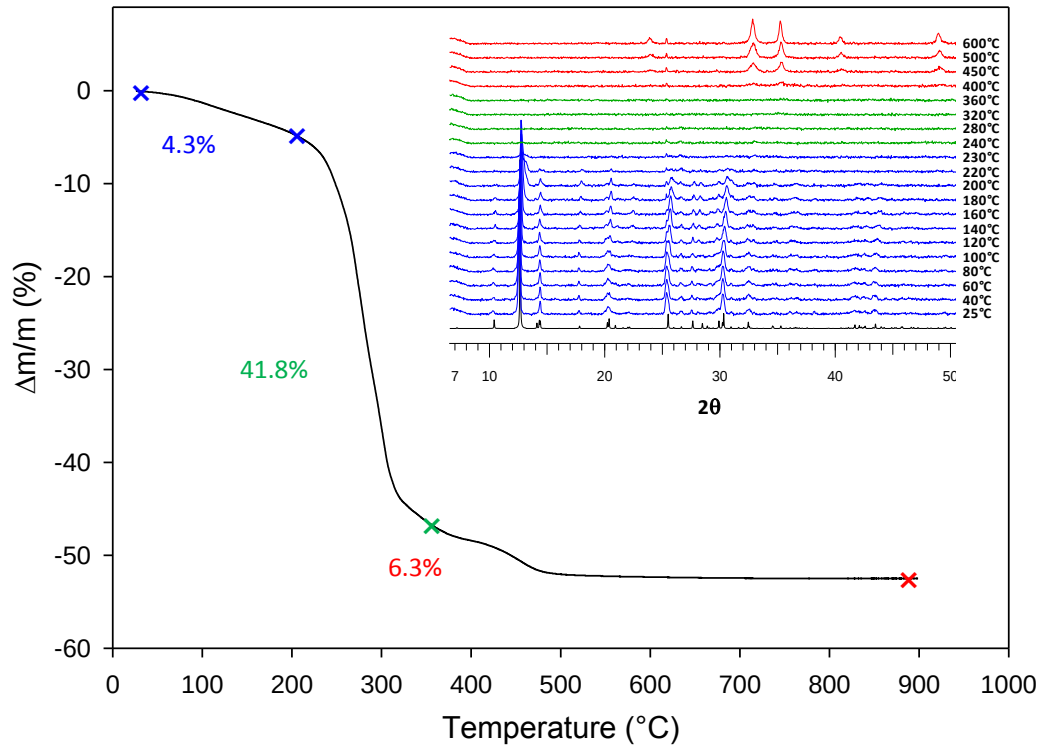

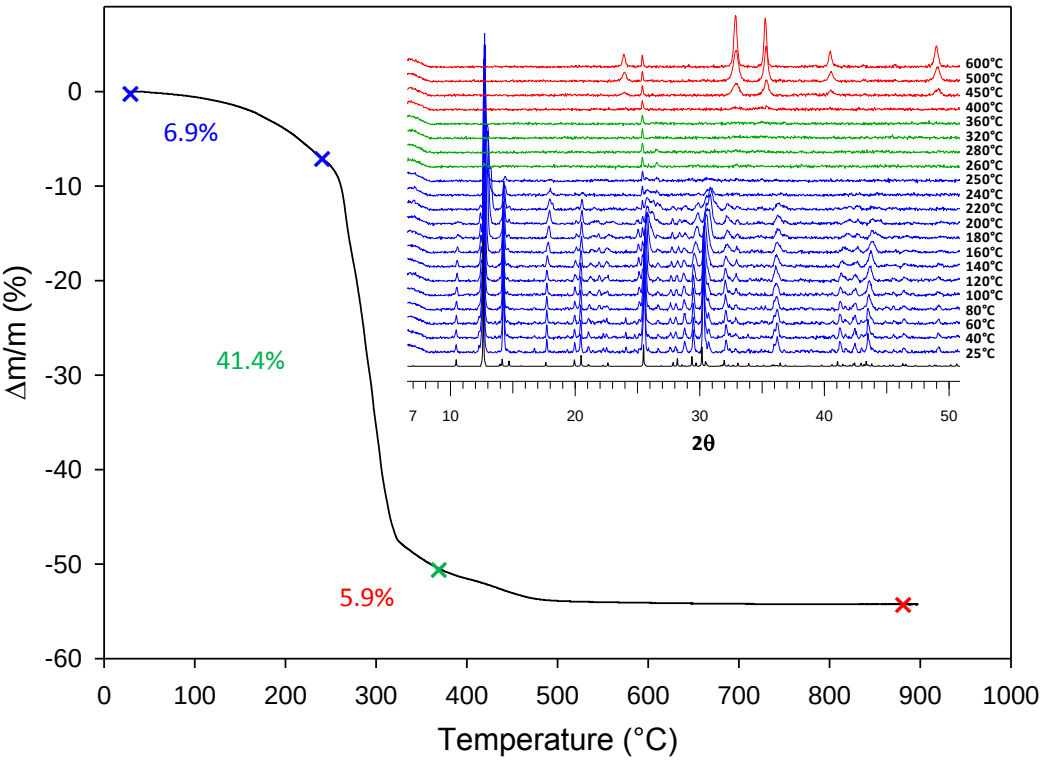

Fig. 6. ^{57}Fe Mössbauer spectra of **1** and **2** recorded at 300 K and 77 K.

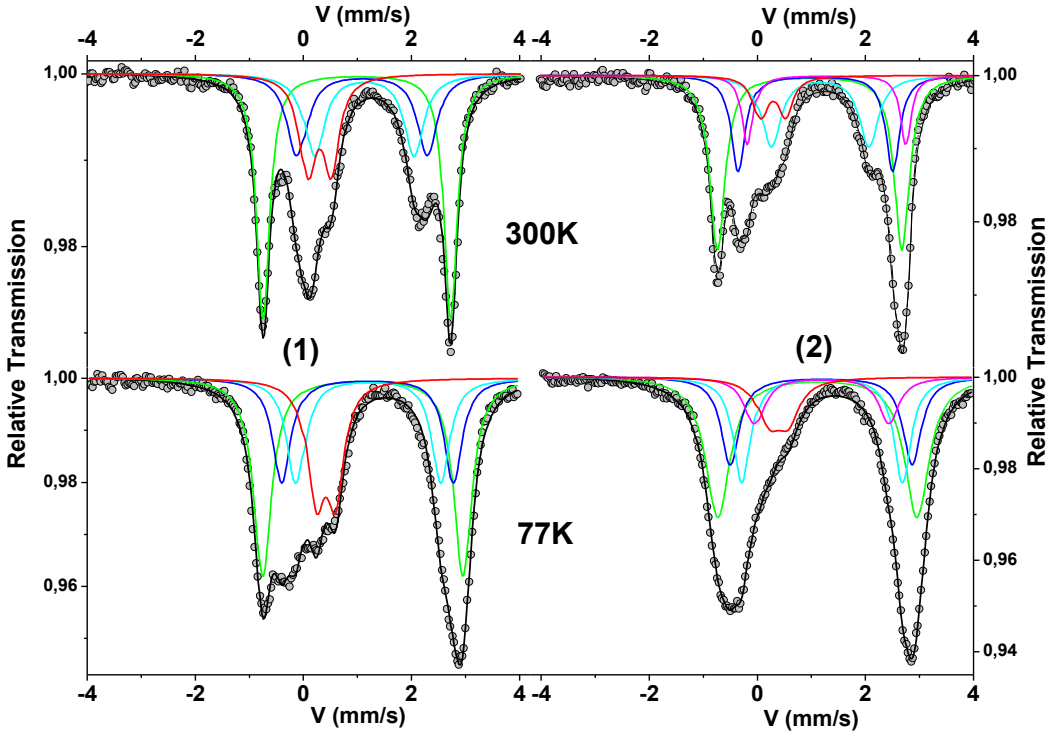

Fig. 7. Zero-field cooled (ZFC) and inverse magnetic susceptibilities of (a) **1** and (c) **2** measured in a 1 T field. The red solid lines are fits to the data described in the text. The insets show the splitting of ZFC and FC susceptibilities at low temperature. The field dependence of the FC susceptibilities of (b) **1** and (d) **2** below 30 K.

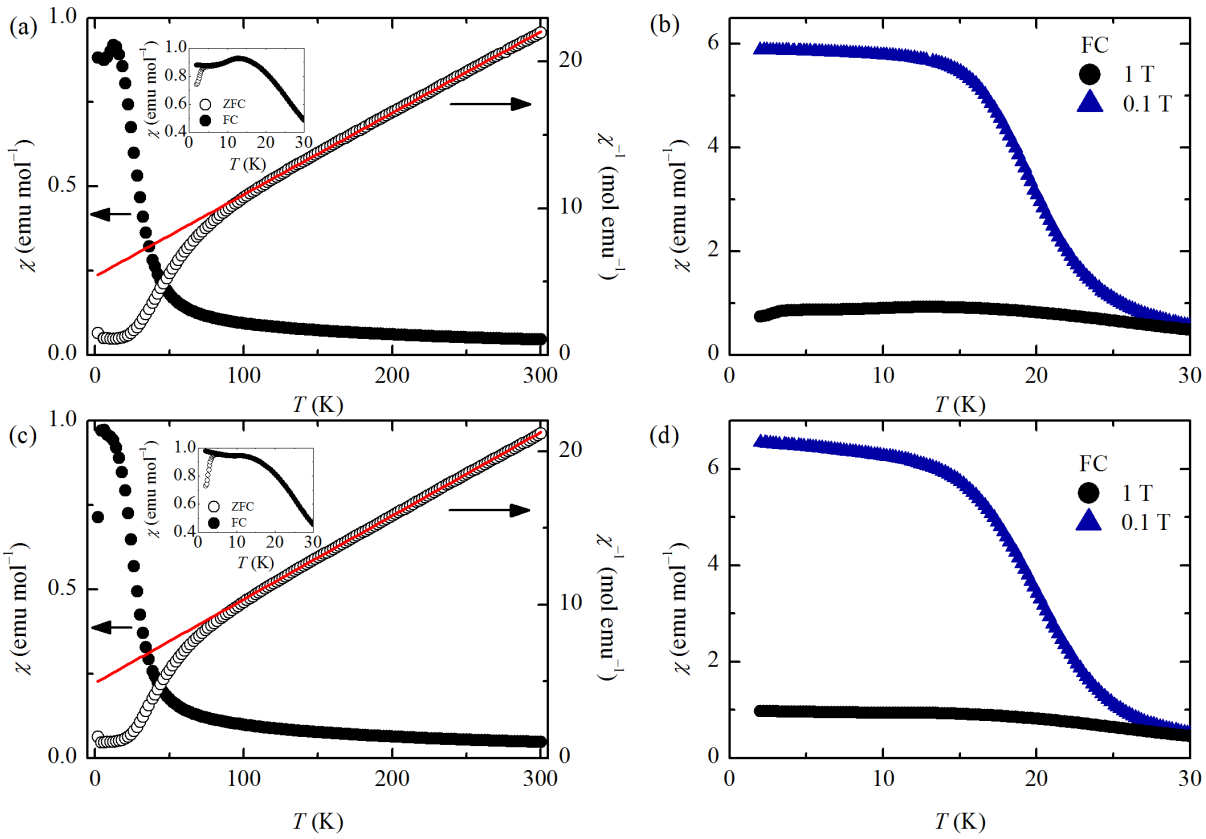

1. L. Mitchell, B. Gonzalez-Santiago, J. P. S. Mowat, M. E. Gunn, P. Williamson, N. Acerbi, M. L. Clarke and P. A. Wright, *Catal. Sci. Technol.*, 2013, **3**, 606-617.
2. L. Murray, M. Dincă and J. R. Long, *Chem. Soc. Rev.*, 2009, **38**, 1294-1314.
3. J.-R. Li, R. J. Kuppler and H.-C. Zhou, *Chem. Soc. Rev.*, 2009, **38**, 1477-1504.
4. A. C. McKinlay, R. E. Morris, P. Horcajada, G. Férey, R. Gref, P. Couvreur and C. Serre, *Angew. Chem. Int. Ed.*, 2010, **49**, 6260-6266.
5. D. J. Tranchemontagne, J. L. Mendonza-Cortés, M. O'Keeffe and O. M. Yaghi, *Chem. Soc. Rev.*, 2009, **38,** 1257-1283.
6. G. Férey, C. Mellot-Draznieks, C. Serre, F. Millange, J. Dutour, S. Surblé and I. Margiolaki, *Science*, 2005, **309**, 2040-2042.
7. F. Millange, N. Guillou, R. I. Walton, J.-M. Grenèche, I. Margiolaki and G. Férey, *Chem. Commun.*, 2008, 4732-4734.
8. W. Ouellette, K. Darling, A. Prosvirin, K. Whitenack, K. R. Dunbarb and J. Zubieta, *Dalton Trans.*, 2011, **40**, 12288-12300.
9. M. Dincă , A. F. Yu and J. R. Long, *J. Am. Chem. Soc.*, 2006, **128**, 8904-8913.
10. C. A. Black, J. Sánchez Costa, W. T. Fu, C. Massera, O. Roubeau, S. J. Teat, G. Aromí, P. Gamez and J. Reedijk, *Inorg. Chem.*, 2009, **48**, 1062-1068.
11. C. Falaise, C. Volkringer and T. Loiseau, *Cryst. Growth Des.*, 2013, **13**, 3225-3231.
12. J. Lhoste, K. Adil, A. Le Bail, M. Leblanc, A. Hémon-Ribaud and V. Maisonneuve, *J. Fluorine Chem.*, 2012, **134**, 29-34.
13. A. Cadiau, C. Martineau, M. Leblanc, V. Maisonneuve, A. Hémon-Ribaud, F. Taulelle and K. Adil, *J. Mater. Chem.*, 2011, **21**, 3949-3951.
14. C. N. R. Rao, S. Natarajan and R. Vaidhyanathan, *Angew. Chem. Int. Ed.*, 2004, **43**, 1466-1496.
15. N. Ahmad, A. H. Chughtai, H. A. Younus and F. Verpoort, *Coord. Chem. Rev.*, 2014, **280**, 1-27.
16. H. Furukawa, K. E. Cordova, M. O'Keeffe and O. M. Yaghi, *Science*, 2013, **341**, 1230444.
17. G. K. H. Shimizu, R. Vaidhyanathan and J. M. Taylor, *Chem. Soc. Rev.*, 2009, **38**, 1430-1449.
18. W. Ouellette, S. Jones and J. Zubieta, *CrystEngComm*, 2011, **13**, 4457-4485.
19. G. Aromi, L. A. Barrios, O. Roubeau and P. Gamez, *Coord. Chem. Rev.*, 2011, **255**, 485-546.
20. R. J. Herr, *Bioorg. Med. Chem.*, 2002, **10**, 3379-3393.
21. H. Zhao, Z.-R. Qu, H.-Y. Ye and R.-G. Xiong, *Chem. Soc. Rev.*, 2008, **37**, 84-100.
22. X. He, C.-Z. Lu and D.-Q. Yuan, *Inorg. Chem.*, 2006, **45**, 5760-5766.
23. X.-W. Wang, J.-Z Chen and J.-H. Liu, *Cryst. Growth Des.*, 2007, **7**, 1227-1229.
24. T. Panda, P. Pachfule, Y. Chen, J. Jiang and R. Banerjee, *Chem. Commun.*, 2011, **47**, 2011-2013.
25. D.-S. Liu, Y. Sui, C.-C. Huang, T.-H. Pan, X.-H. Huang, J.-Z. Chen and X.-Z. You, *Inorg. Chem. Commun.*, 2010, **13**, 762-765.

26. T.-W. Wang, D.-S. Liu, C.-C. Huang, Y. Sui, X.-H. Huang, J.-Z. Chen and X.-Z. You, *Cryst. Growth Des.*, 2010, **10**, 3429-3435.
27. M. Kurmoo, H. Kumagai, M. Akita-Tanaka, K. Inoue and S. Takagi, *Inorg. Chem.*, 2006, **45**, 1627-1637.
28. K. Barthelet, J. Marrot, D. Riou and G. Férey, *Angew. Chem. Int. Ed.*, 2002, **41**, 281-284.
29. G. Darmograi, L. Jouffret, A. Hémon-Ribaud, M. Leblanc, G. Dujardin, V. Maisonneuve and J. Lhoste, *Z. Anorg. Allg. Chem.*, 2014, **640**, 1385-1391.
30. M. E. Medina, Y. Dumont, J.-M. Grenèche and F. Millange, *Chem. Commun.*, 2010, **46**, 7987-7989.
31. M. Smida, J. Lhoste, V. Pimenta, A. Hemon-Ribaud, L. Jouffret, M. Leblanc, M. Dammak, J.-M. Greneche and V. Maisonneuve, *Dalton Trans.*, 2013, **42**, 15748-15755.
32. T. Cottineau, M. Richard-Plouet, J.-Y. Mevellec and L. Brohan, *J. Phys. Chem. C*, 2011, **115**, 12269-12274.
33. B. C. Challis and J. A. Challis, *The chemistry of amides*, ed. J. Zabicky, John Wiley & Sons, 1970.
34. A. A. Paletsky, N. V. Budachev and O. Korobeinichev, *Kinetics and Catalysis*, 2009, **50**, 627-635.
35. G. M. Sheldrick (1986) SHELXS-86: a program for structure solution. Göttingen University, Germany.
36. G. M. Sheldrick (1997) SHELXL-97: a program for crystal structure determination, Göttingen University, Germany.
37. I. D Brown and D. Altermatt, *Acta Crystallogr. B*, 1985, **41**, 244-247.
38. N. E. Brese and M. O'Keeffe, *Acta Crystallogr. B*, 1991, **47**, 192-197.
39. W. Liu and H. Thorp, *Inorg. Chem.*, 1993, **32**, 4102-4105.
40. J.-M. Grenèche, J. Linares, F. Varret, Y. Laligant and G. Férey, *J. Magn. Magn. Mater.*, 1988, **73**, 115-122.
41. G. A. Bain and J. F. Berry, *J. Chem. Educ.*, 2008, **85**, 532.
42. E. Herdtweck, J. Graulich and D. Babel, *Z. Naturforsch. B*, 1990**, 45**, 161-169.
43. C. Frommen, L. Schröder, U. Bentrup, W. Massa and J. Pebler, *Z. Naturforsch. B*, 1995**, 50**, 1627-1637.
44. T. Mahenthirarajah, Y. Li and P. Lightfoot, *Dalton Trans.*, 2009, **17**, 3280-3285.
45. N. Herron, D. L. Thorn , R. L. Harlow and F. Davidson, *J. Am. Chem. Soc.*, 1993, **115**, 3028-3029.
46 A. L. Spek (2002) PLATON: a Multipurpose Crystallographic Tool, Utrecht University, Netherlands.
47. S. Blundell, *Magnetism in condensed matter*, Oxford University Press, 2001.
48. A. P. Ramirez, *Annu. Rev. Mater. Sci*., 1994, **24**, 453-480.